Results in Optics 9 (2022) 100280

Contents lists available at ScienceDirect

Results in Optics

journal homepage: www.sciencedirect.com/journal/results-in-optics

Tuneable blue to orange phosphor from Sm^{3+} doped $ZnAl_2O_4$ nanomaterials

S.P. Khambule [a,*], S.V. Motloung [b,c], T.E. Motaung [d,e], L.F. Koao [f], R.E. Kroon [g], M.A. Malimabe [a,*]

[a] Department of Chemistry, University of the Free State (Qwa Qwa Campus), Private Bag X13, Phuthaditjhaba 9866, South Africa
[b] Department of Chemical and Physical Sciences, Walter Sisulu University, Private Bag X1, Mthatha, South Africa
[c] Department of Physics, Sefako Makgatho Health Sciences University, P. O. Box 94, Medunsa 0204, South Africa
[d] Department of Chemistry, School of Science in the College of Science Engineering and Technology, University of South Africa, Preller Street, Muckleneuk Ridge, City of Tshwane, P. O. Box 392, UNISA, 0003, South Africa
[e] Department of Chemistry, Sefako Makgatho Health Science University, P. O. Box 94, Medunsa 0204, South Africa
[f] Department of Physics, University of the Free State (Qwa Qwa Campus), Private Bag X13, Phuthaditjhaba 9866, South Africa
[g] Department of Physics, University of the Free State (Bloemfontein Campus), P. O. Box 339, Bloemfontein 9300, South Africa

ARTICLE INFO

Keywords:
Co-precipitation
$ZnAl_2O_4$
Sm^{3+}
Dopant
Photoluminescence
Surface defects

ABSTRACT

Undoped and Sm^{3+} doped $ZnAl_2O_4$ nanopowders were synthesized using the co-precipitation method and annealed at 750 ℃ for 3.5 h. The aim of this study was to investigate the effect of varying the Sm^{3+} concentration on the $ZnAl_2O_4$ structure, morphology, and optical properties. The X-ray diffraction analysis confirmed that the samples have a face-centred cubic structure. Crystallite size decreased with an increase in Sm^{3+} concentration. Scanning electron microscopy revealed that the addition of Sm^{3+} slightly influence the morphology of the samples. Transmission electron microscopy confirmed a slight decrease in particle sizes. Energy-dispersive X-ray spectroscopy analysis confirmed the anticipated elemental composition. Ultraviolet–visible spectroscopy showed an increase in bandgap compared to the host. Photoluminescence analysis indicated that doping with Sm^{3+} induced defects within $ZnAl_2O_4$. The emission peaks observed around 380, 401, 451, 500, and 739 nm are attributed to host material. The emission peaks at 564, 601, and 649 nm correspond to the $^5G_{5/2} \rightarrow {}^6H_{5/2}$, $^6H_{7/2}$, and $^6H_{9/2}$ transition of Sm^{3+}, respectively. The highest luminescence intensity was found for the 0.5 % Sm^{3+} sample. The CIE colour chromaticity diagram showed that the emission colour could be tuned from bluish to nearly white to orange.

1. Introduction

Nanostructured functional materials have drawn lots of research attention because of their well-known size, shape, and surface morphology which plays a vital role in controlling the physical, chemical, optical and electronic properties of these nanoscale materials (Li et al., 2021; Tran et al., 2021). Spinel is a class of inorganic materials; these spinel oxides are semiconductors (Sampath et al., 1999; Foletto et al., 2013). Spinels have a general form of AB_2O_4 with different structures (Pathak et al., 2014). Researchers have been interested in these oxides because they have properties like high chemical, thermal stability and high mechanical resistance (Cornu et al., 2014; Ha et al., 2009). The choice of host matrix is an essential key to enhancing the luminescent properties of phosphors (Dhak and Pramanik, 2006). Zinc aluminate ($ZnAl_2O_4$) is a good example of the spinel structure AB_2O_4 belongs to the Fd3m space group (Tran et al., 2021). It has a combination of desirable properties such as high mechanical strength, high thermal and chemical stability (Macedo et al., 2017; Zawadzki et al., 2001). This ternary oxide is used as a sensor, optical, electronic and high-temperature materials (Zawadzki et al., 2001). Crystalline $ZnAl_2O_4$ semiconductors have an optical band gap of ~3.8 eV, and this means that the polycrystalline form of $ZnAl_2O_4$ is transparent to light (Sampath and Cordaro, 2005). Preparation of $ZnAl_2O_4$ has been reported by several physical and chemical methods, namely co-precipitation (Battiston et al., 2014), sol–gel method (Koao et al., 2018), and microwave-hydrothermal method (Macedo et al., 2017) to name a few. In this study,

* Corresponding authors.
E-mail addresses: 2013088964@ufs4life.ac.za (S.P. Khambule), mokoenama@ufs.ac.za (M.A. Malimabe).

https://doi.org/10.1016/j.rio.2022.100280
Received 14 February 2022; Received in revised form 12 July 2022; Accepted 25 July 2022
Available online 28 July 2022
2666-9501/© 2022 Published by Elsevier B.V. This is an open access article under the CC BY-NC-ND license (http://creativecommons.org/licenses/by-nc-nd/4.0/).

the co-precipitation method was preferred because it is easier to control preparation parameters (such as temperature, mixing rate, dopant concentration and pH), therefore producing materials with high purity and fine particle size at a relatively average expense (Ntwaeaborwa et al., 2017; Koao et al., 2018).

The improvement of luminescent materials relies on the host support material as a critical parameter (Mekprasart and Boonyarattanakalin, 2018). It has been outlined that the luminescent properties of phosphors firmly depend on particle size, crystal structure, morphology, and preparation method (Koao et al., 2018). Samarium (Sm^{3+}) can be used as a dopant in different crystal hosts and is an essential luminescent activator (Zhang and Seo, 2011; Hajer et al., 2014). Optimizing the activator incorporated into the host matrix during the phosphor synthesis is critical for creating rare earth ions (RE^{3+}) doped crystalline phosphors with high luminescent effectiveness (Zhang et al., 2013). $ZnAl_2O_4$:Sm^{3+} has unique luminescent properties, which result from the stability and high emission quantum yields (Kumar et al., 2012). Doping with a transition metal (Tm^{3+}) or a RE^{3+}ions, it was demonstrated that the emissions of the $ZnAl_2O_4$-based phosphors could be tunable in the green–red wavelength region (Tran et al., 2021). $ZnAl_2O_4$ doped with Sm^{3+} ions has been investigated by other researchers (Mekprasart and Boonyarattanakalin, 2018; Zhang et al., 2013; Mahajan et al., 2018). In a study by Amjad et al. (Amjad et al., 2012) where lead–zinc phosphate glass was doped with Sm^{3+} ions, they were prepared using the melt-quenching technique excited at 406 nm. In this study, PL spectra display-four elevated emission peaks at 560, 597, 642 and 700 nm, attributed to transitions in the ground $^4G_{5/2}$ and the excited state ^6H_J (J = 5/2; 7/2; 9/2 and 11/2). The authors further concluded that the concentration of Sm^{3+} ions enhanced intensity of emission peaks. Habibi et al. (Habibi et al., 2021) synthesized Ce^{3+} doped $ZnAl_2O_4$:x% Ce^{3+} via the facile co-precipitation method. PL studies show that Ce ions affect the photoluminescence intensity. Therefore when increasing the concentration of Ce ions, the emission peak intensity decreases due to unstable structure. Lamonova et al. (Lamonova et al., 2022) in their synthesis of $MgAl_2O_4$:Sm^{3+} by co-precipitation method reported that Sm^{3+} ions were characterized by 4f transitions and luminescence intensity depended significantly on Sm^{3+} concentration. Kumar et al. (Kumar et al., 2014) synthesized $ZnAl_2O_4$ doped with Sm^{3+} by sol–gel with citric acid as a chelating agent and Mahajan et al. (Mahajan et al., 2018) used solution combustion synthesis route. These reports showed no evidence of how varying Sm^{3+} concentrations modified the host material. This study investigates the influence of Sm^{3+} on $ZnAl_2O_4$ in terms of structure, morphology, optical and luminescent properties at different dopant concentrations. It was fascinating to observe that the Sm^{3+} doped $ZnAl_2O_4$ exhibits emission peaks at around 380, 401, 451, 500, 550 and 739 nm, which were related to the intrinsic defects emissions within the $ZnAl_2O_4$ host material (Amjad et al., 2012). In this work, it was reported for the first time that Sm^{3+} induces more defects such as oxygen vacancies in the $ZnAl_2O_4$ lattice.

Currently, the production of high-quality phosphors for white-light-emitting applications is a hot topic in the phosphor material synthesis research around the world due to the important goals such as; for the light-emitting diodes in the market and possible applications in households (Moji et al., 2020). White light can be generated by adjusting the proportions of the primary colours (blue, red and green). To obtain white light, primary colours should emit at suitable intensities at the same time and to achieve this often multiple doping is used. In other rare cases where only a single RE^{3+} is used to obtain the white light, dopant concentration plays a vital role (Cesaria and Di Bartolo, 2019; He et al., 2009). In this work, the CIE colour chromaticity diagram showed that at a concentration of 1.0 % Sm^{3+}, a white light-emitting phosphor was produced. Increasing the amount of Sm^{3+}, the colour shifted further to orange. This work also reports for the first time the possibility of producing the white light-emitting phosphor from $ZnAl_2O_4$:Sm^{3+}. There are scarce reports on white light colour from the singly doped $ZnAl_2O_4$ host material. This study aims to produce more promising luminescent nanophosphor for practical applications such as light-emitting diode (LED). The perceived emission channels are discussed in detail.

2. Experimental

2.1. Materials

All the chemicals used to prepare the nanopowders were of analytical grade. These include aluminium nitrate [$Al(NO_3)_3{\cdot}9H_2O$] (99.0 %), zinc acetate [$Zn(CH_3CO_2)_2{\cdot}2H_2O$] (99.9 %), samarium acetate [$Sm(CH_3CO_2)_3{\cdot}3H_2O$] (99.9 %), and ammonium hydroxide (NH_4OH) (28 %).

2.2. Preparation of nanopowders

Nanopowders were synthesized by the co-precipitation method and annealed at 750 ℃ for 3.5 h. Annealing improves workability and removes impurities present on the surface of the material. An aqueous solution of zinc acetate (3.69 g and 60 ml H_2O) and aluminium nitrate (12.60 g and 60 ml H_2O) was stirred until fully dissolved. Afterwards, 28 % v/v ammonia solution was added into the zinc/aluminium solution (Zawadzki et al., 2001; Kuhn et al., 2014). The mixture (having a pH of about 8.3–8.5.) was stirred at room temperature until precipitation occurred. The white precipitates were then washed with distilled water, filtered, and left to dry for 48 h at room temperature. Dried samples were crushed into white powders. Synthesis of Sm^{3+} doped $ZnAl_2O_4$ nanopowders was performed similarly by adding different concentrations of samarium acetate to the cation precursor solution. The Sm^{3+} concentration varied as follows: 0.5; 1.0; 2.0 and 3.0 %.

2.3. Characterization

The samples structural analysis was determined by a Bruker AXS D8 Advance diffractometer with Cu Kα (1.5406 Å) radiation in a continuous θ-θ scan in locked coupled mode. The measurements were run within a 2θ range of 10° to 130° but observed at 20° to 80°. Morphology and chemical composition were analyzed using a Tescan Vega3 scanning electron microscope equipped with an Oxford X-Max^N energy dispersive X-ray spectrometer (EDS). Lambda 950 UV–vis spectrometer from Perkin-Elmer using an integrating sphere accessory was used to obtain diffuse reflectance. Photoluminescence (PL) measurements were done with a 325 nm He-Cd laser PL system.

3. Results and discussion

3.1. X-ray diffraction (XRD)

Fig. 1 (a) shows the undoped and Sm^{3+} doped $ZnAl_2O_4$ at varying concentrations, and all diffraction peaks are indexed to the standard data for the cubic phase (JCPDS-05-0669). No other diffraction peaks related to impurities were detected, which suggests that the Sm^{3+} ions are well incorporated into the $ZnAl_2O_4$ lattice sites (Motloung et al., 2015). Thus, the results suggest that Sm^{3+} is incorporated successfully into the crystal structure $ZnAl_2O_4$. Fig. 1 (b) represents the magnified version of the most intense (3 1 1) diffraction peak. The results show that the peak intensity decreased with an increase in the dopant concentration, which can be attributed to the decrease in crystalline quality or degree of crystallinity (Mekprasart and Boonyarattanakalin, 2018; Farhadi and Panahandehjoo, 2010; Koao et al., 2016). The diffraction peaks shift slightly toward lower angles with an increase in the dopant ions as shown in Fig. 1(b), indicating that the lattice parameters are slightly larger than those of undoped $ZnAl_2O_4$, which is mainly due to larger radius of Sm^{3+} than that of Zn^{2+} and Al^{3+}. This indicating that the dopant ions are well incorporated into the lattice sites of Zn^{2+} or Al^{3+} and lead to the increase in inter atomic distance (Koao et al., 2014).

According to Fig. 1(a), the (311) diffraction peak has the highest

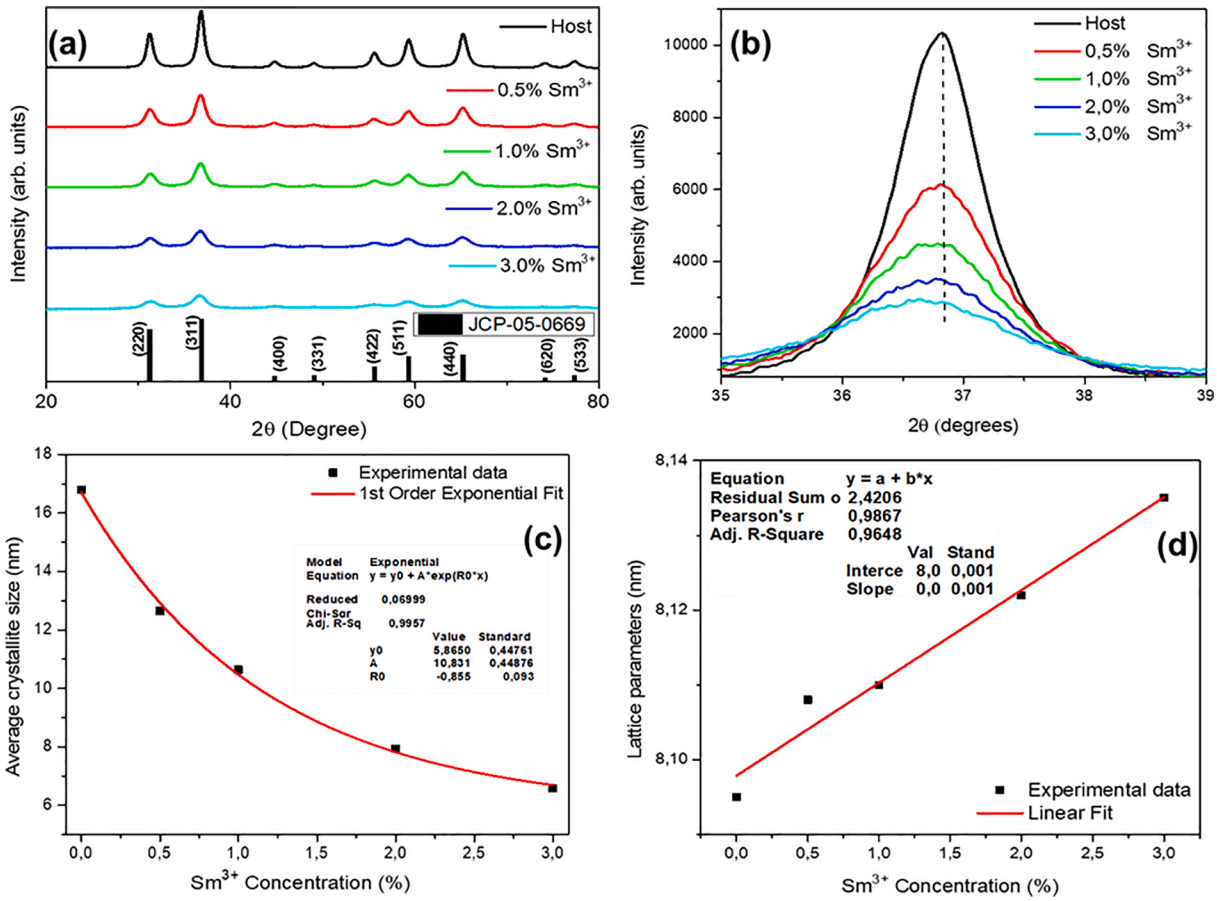

Fig. 1. (a) XRD patterns of undoped and Sm^{3+} doped $ZnAl_2O_4$ nanopowders, (b) Zoomed version of the (311) diffraction peak, (c) Average crystallite size as a function of the concentrations of Sm^{3+} ions, (d) Lattice parameter versus the concentrations of Sm^{3+} ions.

intensity. Since grains are expected to have random orientation, therefore the intensities correlate with those from the JCPDS powder standard that indicates a random orientation (Bunge, 1997). The Scherrer equation was used to estimate the average crystallite sizes (D)

$$D = \frac{k\,\lambda}{\beta\cos\theta} \tag{1}$$

where the D was estimated from full-width at half-maximum (β), k is the crystallite shape factor (0.9) using the most intense (311) diffraction peak at angle θ. The values are displayed in Table 1, and the crystallite size as a function of Sm^{3+} concentration is shown in Fig. 1(c). It can be observed that there is generally a gradual decrease in crystallite size with an increase in Sm^{3+} concentration. Faraz et al. (Faraz et al., 2018) found that the reduction of crystallite size is due to the distortion in the ZnO lattice when increasing the Sm^{3+} concentration, which is responsible for decreasing the nucleation and subsequent growth rate of the ZnO nanoparticles (Faraz et al., 2018). It is also possible that the distortion also occurs in the Sm^{3+} doped $ZnAl_2O_4$ system.

The lattice parameter (a) for the cubic material was estimated using equation (2) (Koao et al., 2018):

$$a = d_{hkl}\sqrt{h^2 + k^2 + l^2} \tag{2}$$

The values are presented in Table 1. Fig. 1(d) shows the a as a function of the Sm^{3+} concentration. It is clear that lattice parameters (a and d) increases with an increase in Sm^{3+} concentration. This increase is due to a large ionic radius of Sm^{3+} (0.964 Å) compared to Zn (0.74 Å) and Al (0.533 Å). The increase in lattice parameters is attributed to the replacement of the smaller atoms with the bigger atom in the crystal lattices of the individual phases. When the smaller ions (Zn^{2+} or Al^{3+}) are replaced by the larger Sm^{3+} ion, this will result in an increase in lattice parameter. Thus, we propose that the Sm^{3+} ions substitute the Zn^{2+} or Al^{3+} ions in the crystal lattice $ZnAl_2O_4$ (Mhlongo et al., 2019).

Table 1
Parameters of the $ZnAl_2O$. Sm nanopowders using the (311) diffraction peak and bandgap energy.

Sm^{3+} concentration/%	a/Å	2θ/°	β/rad	d/Å	D/ nm	Bandgap Energy/eV
Undoped	8.09	36.79 ± 0.01	0.0082	2.44	17	3.27
0.5	8.10	36.77 ± 0.02	0.0109	2.44	13	3.30
1.0	8.11	36.72 ± 0.02	0.0125	2.45	11	3.31
2.0	8.12	36.67 ± 0.02	0.0141	2.45	8	3.32
3.0	8.14	36.60 ± 0.02	0.0163	2.45	7	3.33

3.2. Scanning electron microscopy (SEM)

The surface morphology of the undoped and Sm^{3+} doped $ZnAl_2O_4$ is shown in Fig. 2 to ascertain the effect of Sm^{3+} ions. In Fig. 2(a), the host displayed non-uniform spherical structures with irregular particle size distribution across a rough surface. Fig. 2(b-e) show 0.5 %, 1.0 %, 2.0 % and 3.0 % of Sm^{3+}; these micrographs showed the agglomeration of small spherical structures and a homogenous distribution. Faraz et al. (Faraz et al., 2018) reported a similar morphology for Sm^{3+} doped ZnO nanoparticles and outlined that the doped nanoparticles showed a

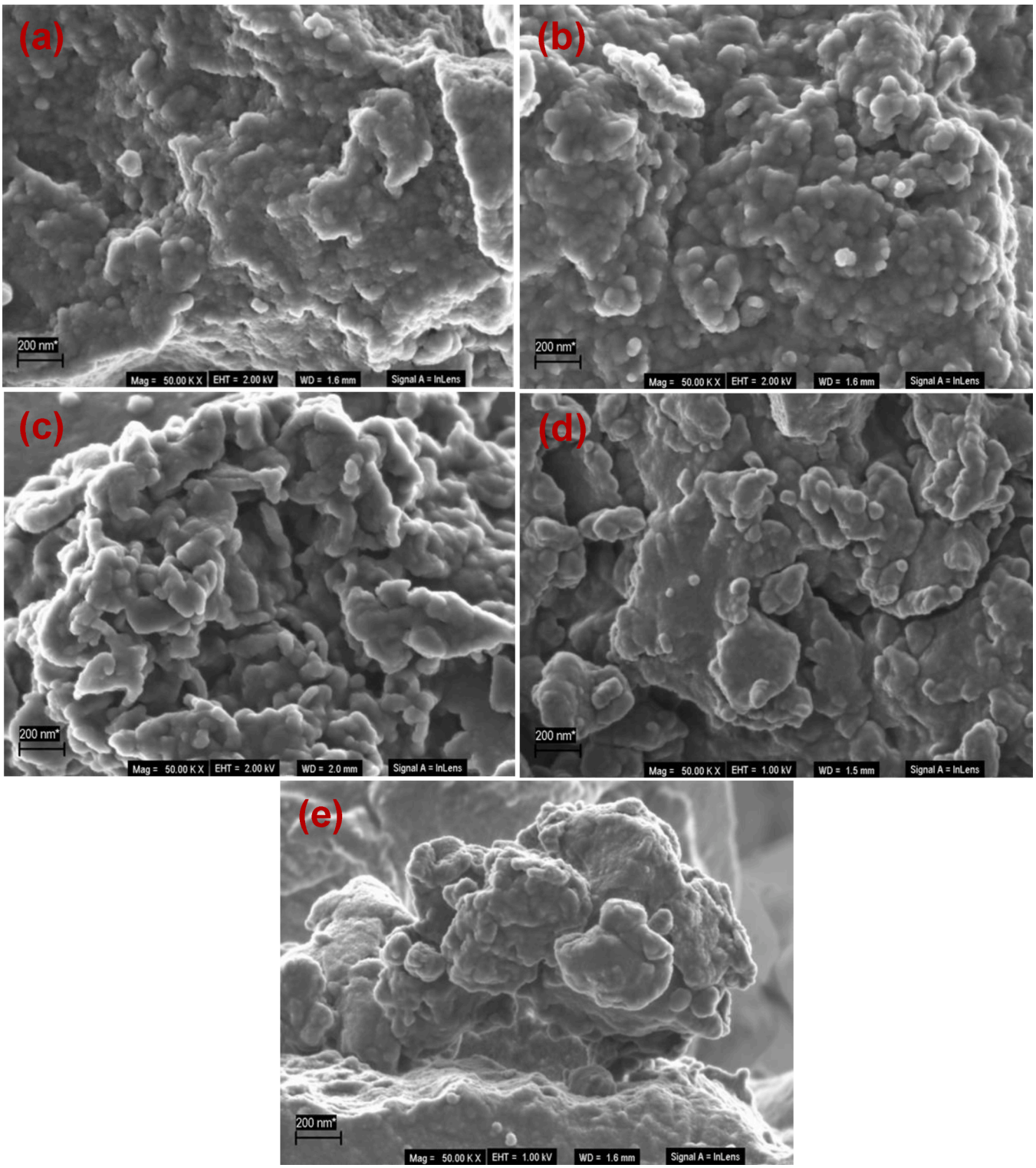

Fig. 2. SEM micrographs of (a) Undoped $ZnAl_2O_4$; (b) 0.5 % of Sm^{3+}; (c) 1.0 % of Sm^{3+}; (d) 2.0 of % Sm^{3+}.and (e) 3.0 of % Sm^{3+}.

homogenously spherical morphology. Motloung et al. (Motloung et al., 2017) also found that doping $ZnAl_2O_4$ with Cu^{2+} resulted in the agglomeration of irregular spherical structures. The spherical structures were slightly reducing in terms of size with an increase in the amount of Sm^{3+}. The observed behavior agrees with the decreasing crystallite size observed in XRD. At high concentration of Sm^{3+} (3.0 %) the irregular spherical particles are slightly disappearing. In addition, a slight change in morphology is attributed to an increase in dopant concentration and difference in ionic radius. The Sm^{3+} ions are much bigger than the Zn^{2+} and Al^{3+} ions (Koao et al., 2016; Motloung et al., 2017) and therefore, incorporation is likely to be challenging. Therefore, the large difference in ionic radius makes incorporation difficult, creating large strains and causing the Sm^{3+} ions to have a notable effect on the host morphology.

The SEM selected samples were further analysed by the TEM to investigate the phase change, crystal size and shapes. The TEM images of the selected samples are depicted on Fig. 3. In general, the TEM images

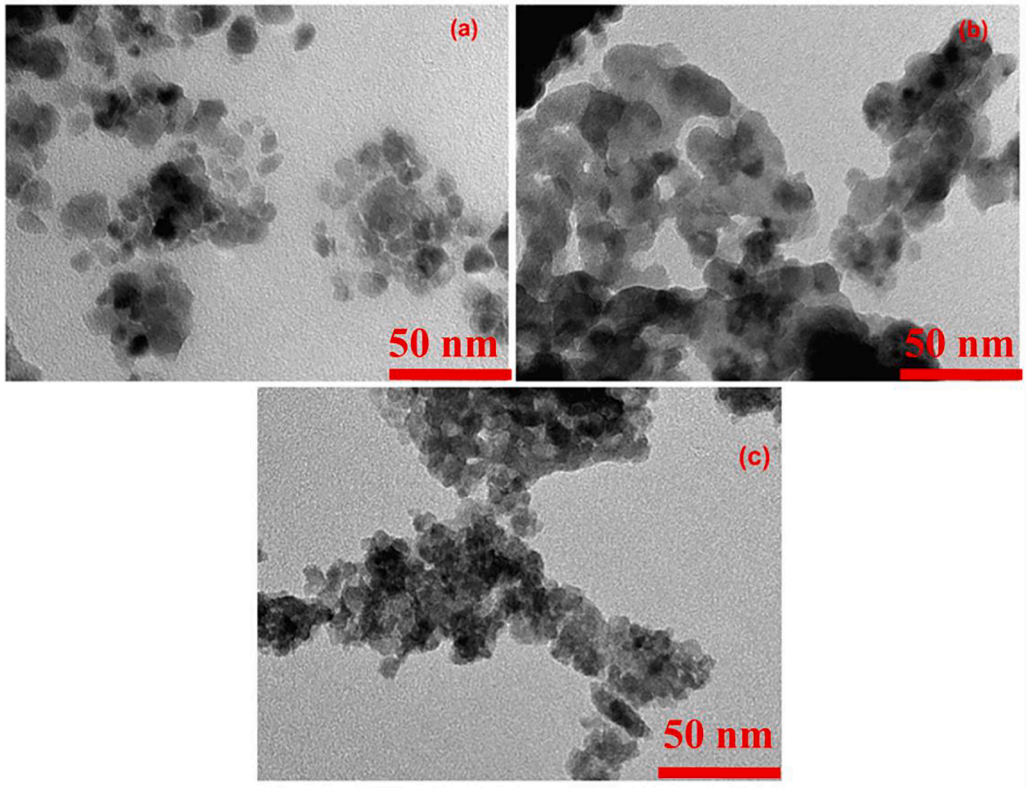

Fig. 3. TEM images of (a) Undoped $ZnAl_2O_4$; (b) 0.5 % of Sm^{3+}; and (e) 3.0 of % Sm^{3+}.

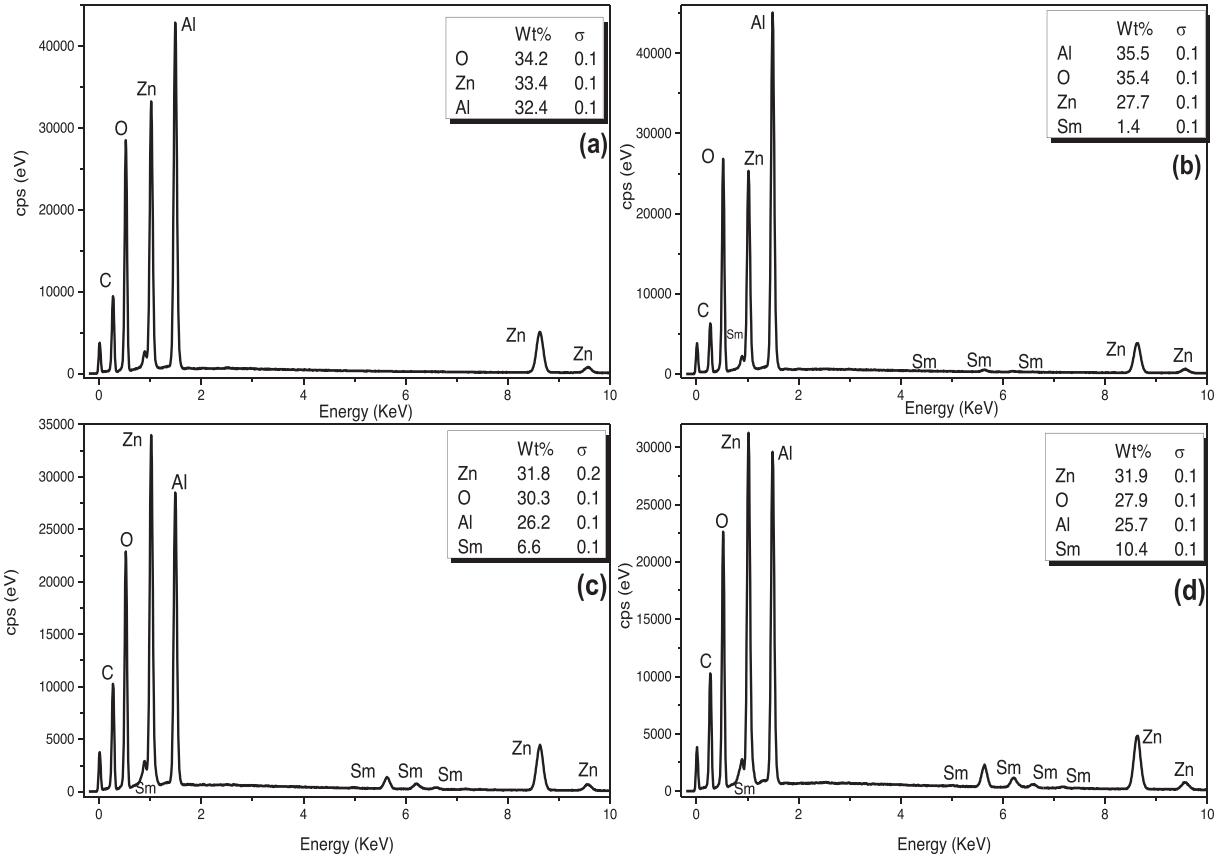

Fig. 4. EDS spectra of the (a) undoped $ZnAl_2O_4$, (b) 0.5 % Sm^{3+}, (c) 2.0 % Sm^{3+}, and (d) 3.0 % Sm^{3+}.

confirm what has been observed in SEM in terms of morphology. It was also noted a decrease in crystallite sizes at high concentration of Sm^{3+} (3.0 %). This agrees with XRD and SEM analysis. The estimated average values of the crystallite sizes was 11 nm using Fig. 3(a) and (b), which confirms the values estimated in the XRD results in Table 1. In Fig. 3(c) it was very difficult to estimate the crystallite sizes since they are very small and agglomerated.

3.3. Energy-dispersive X-ray spectroscopy (EDS)

The EDS spectra of the undoped and Sm^{3+} doped $ZnAl_2O_4$ are shown in Fig. 4. It confirmed the presence of Zn, Al, O in the undoped and Sm in the Sm^{3+} doped $ZnAl_2O_4$ nanopowders. The carbon (C) peak observed is from both the carbon tape used to mount the sample and the coating (Mhlongo et al., 2019).

3.4. Optical properties

Fig. 5(a) illustrates the reflectance spectra of undoped and Sm^{3+} doped $ZnAl_2O_4$ samples, for a spectral range of 300–650 nm. The absorption edge for undoped $ZnAl_2O_4$ was observed at around 348 nm. The observed absorption is due to the band-to-band transition of AlO_6 anion grouping in $ZnAl_2O_4$ (Koao et al., 2018; Motloung et al., 2015). For the Sm^{3+} doped $ZnAl_2O_4$ nanopowders, the absorption edge shifted to moderately high wavelength from 348 to 358 nm, which might be due to the presence of defect states and disorder due to Sm^{3+} doping (Motloung et al., 2015). The 392, 464, and 548 nm narrow peaks are due to defects-related transitions $^6H_{5/2} \rightarrow {}^6P_{7/2}$, $^6H_{5/2} \rightarrow {}^4F_{5/2} + {}^4I_{13/2}$, and $^6H_{5/2} \rightarrow {}^4G_{5/2}$ of Sm^{3+} ions (Sampath et al., 1999; Sameera et al., 2019). These peaks are increasing when increasing the concentration of Sm^{3+} and that is attributed to Sm^{3+} ions being shielded by the 5 s and 5p filled shells (Selvi et al., 2015).

Fig. 5(b) shows the estimated energy bandgap (E_g) of the nanopowders calculated using the Kubelka-Munk function (Molefe et al., 2014; Motloung et al., 2016). The E_g of the undoped and Sm^{3+} doped $ZnAl_2O_4$ samples can be determined from plots of $(Khv)^2$ versus hv using the Tauc relation (Sameera et al., 2019). It can be clearly seen that the E_g increased when doping with Sm^{3+}. The estimated E_g as a function of Sm^{3+} is shown in Table 1 and Fig. 5(c). The increase in E_g may be due to an observed change in surface morphology from SEM analysis (Motloung et al., 2015; Motloung et al., 2014). Additionally, an increase in E_g can be attributed to the reduction of crystallite size as observed in XRD (Koao et al., 2016). Lastly, the observed increase in E_g of $ZnAl_2O_4$ with increasing dopant corresponds to enhancement of optical absorption spectra (Rahman et al., 2015). Doping with Sm^{3+} significantly influenced the E_g at both low and high Sm^{3+} concentrations.

3.5. Photoluminescence (PL)

The PL measurements of the undoped and Sm^{3+} doped $ZnAl_2O_4$ nanoparticles were carried out at room temperature using the He-Cd laser with an excitation wavelength of 325 nm. The deconvolution of

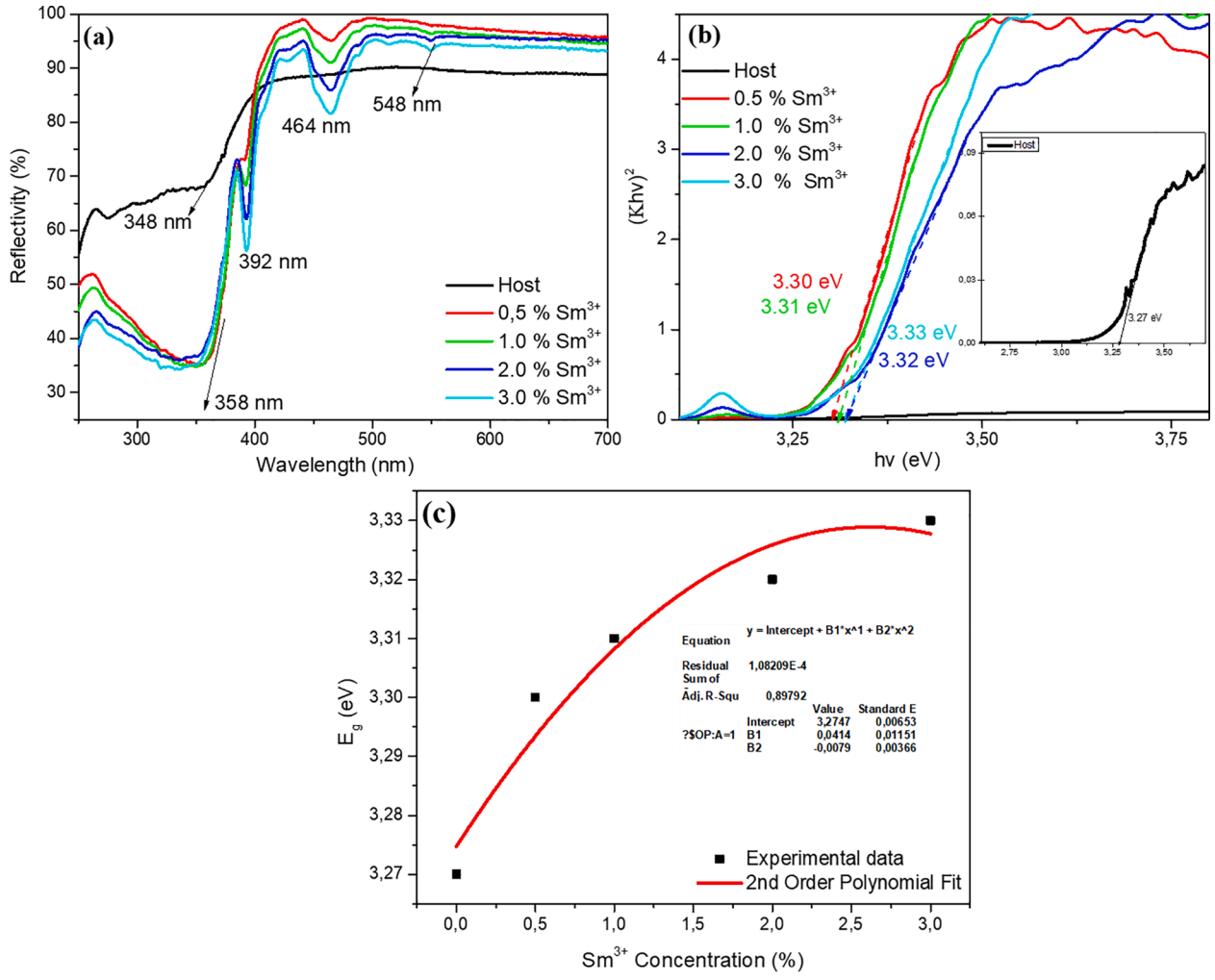

Fig. 5. (a). UV–vis reflectance spectra, (b) Plot to determine the bandgap of the undoped and Sm^{3+} doped $ZnAl_2O_4$ nanopowders and (c) E_g as a function of Sm^{3+} concentration.

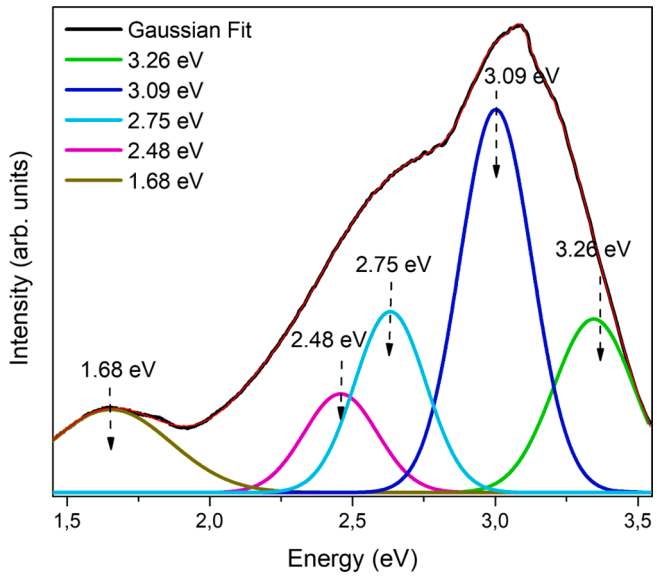

Fig. 6. The deconvolution of the emission of $ZnAl_2O_4$ nanopowder.

the undoped $ZnAl_2O_4$ is shown in Fig. 6. The undoped $ZnAl_2O_4$ nanoparticles exhibited a broad asymmetric band between 3.5 and 1.5 eV. The broad maximum emission peak at around 3.09 eV is assigned to the intrinsic intra-bandgap defects such as oxygen vacancies (V_o) of the $ZnAl_2O_4$ nanoparticles (Motloung et al., 2017). Deconvolution indicated a broad band composed of 3.26 (violet), 3.09 (violet), 2.75 (blue), 2.48 (green), and 1.68 eV (red). The 3.26 eV is due to the band-to-band transition of the AlO_6 anion grouping of $ZnAl_2O_4$ (Motloung et al., 2015). The violet emission at 3.09 eV originates from V_o as stated above, and the blue emission at 2.75 eV is also due to V_o (Koao et al., 2021; Dlamini et al., 2020; Motloung et al., 2019). The red emission at around 1.68 eV was due to transitions associated with oxygen interstitials (O_i) (Koao et al., 2018; Koao et al., 2021; Tangcharoen et al., 2019). Nevertheless, the peak at around 2.48 eV is due to zinc vacancies (V_{Zn}) (Motloung et al., 2015). The 3.26, 2.75 and 2.48 eV peaks are hardly reported.

The PL emission spectra of the $ZnAl_2O_4$ nanostructures in different concentrations of Sm^{3+} are shown in Fig. 7. The results revealed that Sm^{3+} ions affect both luminescence intensity and wavelength. At low dopant concentration, the host emissions (380, 401 and 500 nm) are strongly quenched, and there are weak characteristics of Sm^{3+} emission peaks. As dopant concentration increases, the emission peaks also heighten. Broad emission bands occur over the visible region, which could be caused by defects created by doping (Kumar et al., 2014).

Additionally, the peak shift at 739 nm fluctuates from lower to higher wavelengths with an increase in the amount of Sm^{3+}. This shift to a higher or lower wavelength may be due to the crystal field splitting adjustment (Motloung et al., 2019). Secondly, the shift to lower or higher wavelength may be due to the change in morphology confirmed by SEM analysis (Koao et al., 2016; Koao et al., 2021). Lastly, the shift to a lower wavelength may also be due to a decrease in crystallite size detected in XRD analysis with an increase in Sm^{3+} concentration (Koao et al., 2018; Hile et al., 2021). The luminescence band at around 739 nm increases in intensity until it reaches 1.0 % Sm^{3+}, after which it decreases. As dopant concentration increases, it was noted that there is an emergence of various dopant emissions. These narrow emission peaks are observed at 564, 600 and 649 nm and are attributed to $^4G_{5/2} \rightarrow {}^6H_J$ (J = 5/2; 7/2; and 9/2) transitions (Zhang et al., 2013; Mahajan et al., 2018; Faraz et al., 2018). Biswas et al. (Biswas et al., 2017) revealed that these narrow peaks (568, 600, 649) represent transitions of $^4G_{5/2} \rightarrow {}^6H_{5/2}$ and $^4G_{5/2} \rightarrow {}^6H_{7/2}$ which are magnetic dipole (MD) and $^4G_{5/2} \rightarrow {}^6H_{9/2}$ which is an electric dipole (ED) transition (Amjad et al., 2012; Biswas et al., 2017). Mekprasart et al. (Mekprasart and Boonyarattanakalin, 2018) indicated that Sm^{3+} emission spectra are produced in the red–orange region at three prominent peaks around 565, 601 and 645 nm. The peak at around 688 nm is insignificant because of the laser machine default.

Fig. 8 shows the emission intensity for 380, 401 and 601 nm as a function of Sm^{3+} concentration. Peaks 380 and 401 nm displayed a decrease in luminescent intensity, and because these emission peaks are point defect related, they are associated with a change in defect concentration and quenching (Ntwaeaborwa et al., 2017; Zhang and Lin, 2012). Motloung et al. (Motloung et al., 2015) mentioned that "concentration quenching" is due to new defects sites, which improves non-radiative relaxation (NRR) of excited electrons. Therefore, doping with Sm^{3+} resulted in new defect sites. The emission peak 601 nm was enhanced significantly with an increase in the Sm^{3+} concentration. As Sm^{3+} is doped into $ZnAl_2O_4$, it substitutes the Zn^{2+} and Al^{3+} crystal lattice site, resulting in expansion of the unit cell (Li et al., 2017) due to Sm^{3+} as was observed in XRD. Since this peak is from Sm^{3+} emission transitions, adding Sm^{3+} into the $ZnAl_2O_4$ material enhanced the luminescent intensity.

Fig. 9 shows the proposed emission pathway mechanism for the undoped and Sm^{3+} doped $ZnAl_2O_4$ nanopowders. The luminescence mechanism of the undoped shown in Fig. 9(a) can be elucidated as

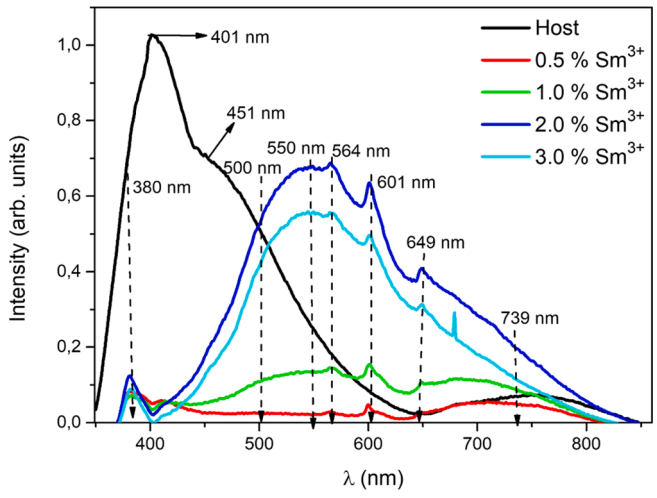

Fig. 7. Emission spectra of the undoped and Sm^{3+} doped $ZnAl_2O_4$ nanopowders.

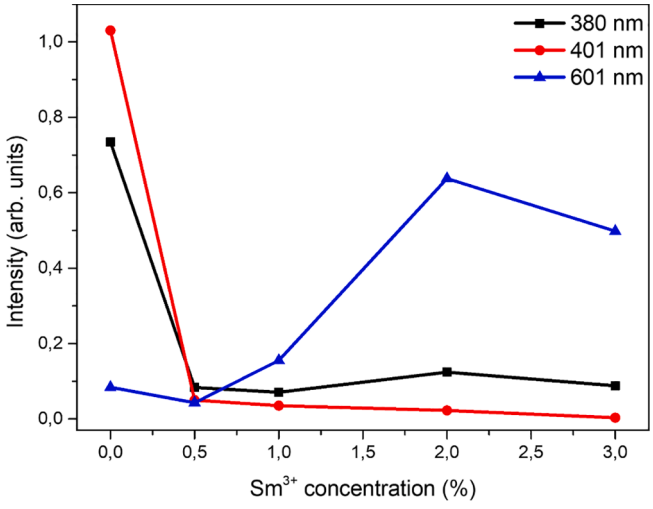

Fig. 8. Intensity versus the concentration of Sm^{3+} ions at 380 nm, 401 and 601 nm.

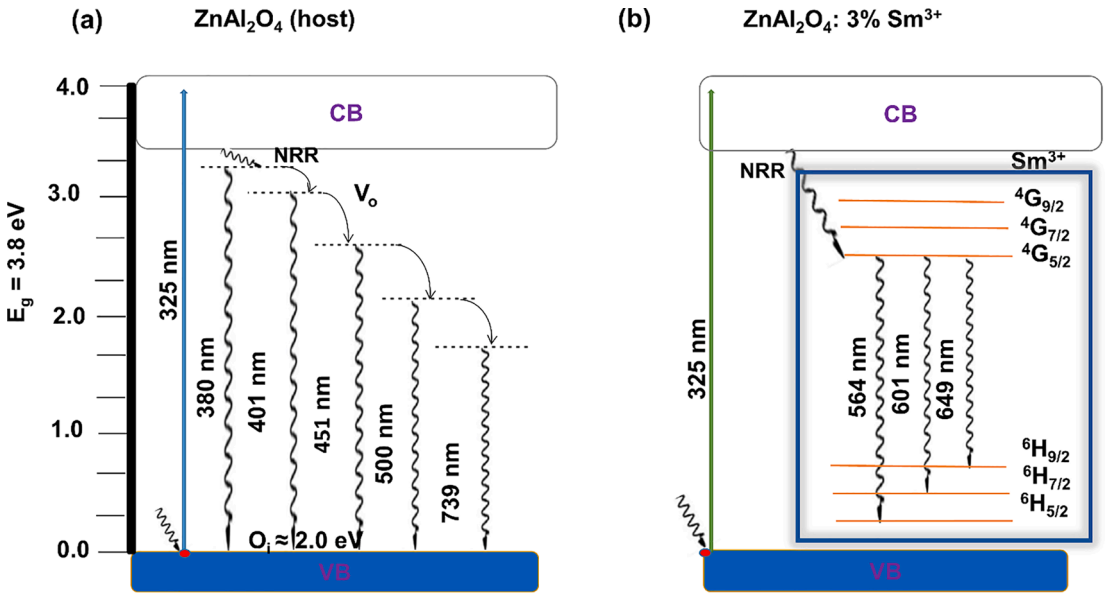

Fig. 9. Emission pathway of (a) Undoped $ZnAl_2O_4$, (b) 3.0 % of Sm^{3+} excited at 325 nm (Deepa et al., 2016).

follows; after exciting at 325 nm (3.8 eV), the electrons (shown in red) in the valence band (VB) are excited to the conduction band (CB). These excited electrons are de-excited by NRR and get trapped in the $ZnAl_2O_4$ defective state (Koao et al., 2018; Dlamini et al., 2020; Motloung et al., 2015). The excitation photon of wavelength 325 nm has energy ~3.8 eV, which is sufficient to promote an electron from the VB to the CB easily. By exciting with 325 nm, the excitation energy goes within the CB and gives emissions shown. The development of new defect states into the $ZnAl_2O_4$ matrix is attributed to the incorporation of Sm^{3+} ions. The emission mechanism of the Sm^{3+} ion shown in Fig. 9(b) outlines that the emission from the Sm^{3+} ions can arise from excited energy levels to its ground states (Motloung et al., 2016).

Fig. 10 shows the CIE diagram of undoped and Sm^{3+} doped $ZnAl_2O_4$ samples excited at 325 nm. The OSRAM CIE colour calculator software (Hebbar et al., 2018, Li and Van Deun, 2018) was used to determine the × and y co-ordinates of the samples. From the host up to 1.0 % Sm^{3+} there is a colour shift from violet to near white. In addition, increasing amount of Sm^{3+} from 1.0 to 3.0 % Sm^{3+} the CIE shifts from near white to reddish-orange. Motloung et al. (Motloung et al., 2015) reported a similar colour tuning when $ZnAl_2O_4$ doped with Eu^{3+}. It can be concluded that adding and varying Sm^{3+} does have an influence on the emission colour.

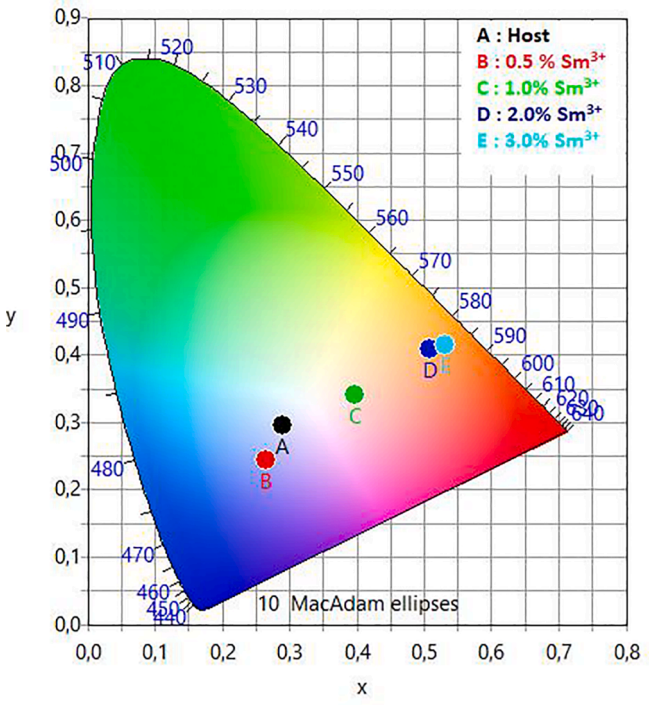

Fig. 10. The CIE chromaticity diagram for the undoped and Sm^{3+} doped $ZnAl_2O_4$.

4. Conclusion

The undoped and Sm^{3+} doped $ZnAl_2O_4$ samples were synthesized by the co-precipitation technique at room temperature and annealed at 750 ℃ for 3 5 h. XRD revealed a pure cubic crystalline structure and Sm^{3+} had a considerable influence on the crystal growth. The average crystallite sizes for undoped $ZnAl_2O_4$ was ~17 nm. It was found that the average crystallite size decreases with increasing Sm^{3+} concentration. Images from SEM and TEM micrographs reveal a similar morphology in agreement with XRD measurements. The E_g can be tuned with increasing dopant concentration, which in turn increases E_g of host and therefore is attributed to presence of defects. PL shows that Sm^{3+} affects the luminescence intensity and wavelength when increasing the concentration of Sm^{3+}. It was reported that the emission intensity is strongly dependant on the concentration of Sm^{3+}, which agrees with the XRD lattice parameter and SEM. It was also observed that Sm^{3+} emit a reddish-orange light which was confirmed by CIE. Lastly, CIE chromaticity diagram displayed colour shift from the violet into reddish-orange region varying Sm^{3+} concentration. It was interesting to observe the dopant concentration 1.0 % Sm^{3+}, to be closest to the white-light. There are limited reports on white light emission for the $ZnAl_2O_4$ doped at different amounts of Sm^{3+}. In this work, it was reported for the first time that the incorporation of Sm^{3+} into $ZnAl_2O_4$ could promote formation of more defects in the $ZnAl_2O_4$ lattice that are due to the host and doping results in altercations of E_g. This work will assist in optoelectric sensors, optical devices, and luminescent materials that emit white light.

Declaration of Competing Interest

The authors declare that they have no known competing financial interests or personal relationships that could have appeared to influence

the work reported in this paper.

Acknowledgements

The authors would like to acknowledge the National Research Foundation (NRF) (fund numbers. UID118492 and UID 99224), the University of the Free State, and NRF incentive funding for rated researchers (IPRR) (Grant No: 126914) for their financial support.

References

Amjad, R.J., Sahar, M.R., Ghoshal, S.K., Dousti, M.R., Riaz, S., Tahir, B.A., 2012. Chinese Phys. Lett. 29, 087304.
Battiston, S., Rigo, C., Severo,, E.da C., Mazutti, M.A., Kuhn, R.C., Gündel, A., Foletto, E. L., 2014. Mater. Res. 17, 734.
Biswas, P., Kumar, V., Padha, N., Swart, H.C., 2017. J. Mater. Sci. Mater. Electron. 28, 6159.
Bunge, H.J., 1997. Textures Microstruct. 29, 1.
Cesaria, M., Di Bartolo, B., 2019. Nanomaterials 9, 1.
Cornu, L., Duttine, M., Gaudon, M., Jubera, V., 2014. J. Mater. Chem. C 2, 9512.
Deepa, A.V., Priya, M., Suresh, S., 2016. Sci. Res. Essays 11, 57.
Dhak, D., Pramanik, P., 2006. J. Am. Ceram. Soc. 89, 1014.
Dlamini, C., Mhlongo, M.R., Koao, L.F., Motaung, T.E., Hlatshwayo, T.T., Motloung, S.V., 2020. Appl. Phys. A 126, 1.
Faraz, M., Naqvi, F.K., Shakir, M., Khare, N., 2018. New J. Chem. 42, 2295.
Farhadi, S., Panahandehjoo, S., 2010. Appl. Catal. A Gen. 382, 293.
Foletto, E.L., Sallet, D., Stringhini, F.M., Bertuol, D.A., do Nascimento, C.A.O., Chiavone-Filho, O., 2013. J. Alloys Compd. 588, 305.
Ha, L.H., Lanh, P.T., Long, N.N., Loan, T.T., 2009. J. Phys. Conf. Ser. 187, 012053.
Habibi, M.K., Rafiaei, S.M., Alhaji, A., Zare, M., 2021. J. Mol. Struct. 1228, 129769.
Hajer, S.S., Halimah, M.K., Azmi, Z., Azlan, M.N., 2014. Chalcogenide Lett. 11, 553.
He, G., Guo, D., He, C., Zhang, X., Zhao, X., Duan, C., 2009. Angew. Chemie 2, 6248.
Hebbar, D.N., Menon, S.G., Choudhari, K.S., Shivashankar, S.A., Santhosh, C., Kulkarni, S.D., 2018. J. Am. Ceram. Soc. 101, 800.
Hile, D.D., Swart, H.C., Motloung, S.V., Motaung, T.E., Kroon, R.E., Egbo, K.O., Pawade, B., Koao, L.F., 2021. Mater. Chem. Phys. 262, 124303.
Koao, L.F., Dejene, F.B., Kroon, R.E., Swart, H.C., 2014. J. Lumin. 147, 85.
Koao, L.F., Dejene, B.F., Swart, H.C., Motloung, S.V., Motaung, T.E., 2016. Opt. Mater. (Amst). 60, 294.
Koao, L.F., Hlatshwayo, T.T., Kumari, P., Motaung, T.E., Mochane, M.J., Motloung, S.V., 2018. Mater. Today Commun. 14, 294.
Koao, L.F., Dejene, B.F., Hone, F.G., Swart, H.C., Motloung, S.V., Motaung, T.E., Pawade, V.B., 2018. J. Lumin. 200, 206.
Koao, L.F., Motloung, S.V., Wesley-Smith, J., Motaung, T.E., Malevu, T.D., Pawade, V.B., Hone, F.G., 2021. J. Alloys Compd. 863, 158367.
Kuhn, R.C., Mazutti, M.A., Battiston, S., Gündel, A., Rigo, C., Foletto, E.L., Severo, E.da C., 2014. Mater. Res. 17, 734.
Kumar, M., Seshagiri, T.K., Mohapatra, M., Natarajan, V., Godbole, S.V., 2012. J. Lumin. 132, 2810.
Kumar, M., Mohapatra, M., Natarajan, V., 2014. J. Lumin. 149, 118.
Kumar, M., Natarajan, V., Godbole, S.V., 2014. Bull. Mater. Sci. 37, 1205.
Lamonova, K., Danilenko, I., Volkova, G., Orel, S., Pashkevich, Y., Prokhorov, A., Viagin, O., Maksimchuk, P., Seminko, V., Malyukin, Y., Kurnosov, V., 2022. J. Lumin. 241, 118493.
Li, G., Liu, G., Mao, Q., Du, G., Li, X., Zhu, Y., Yang, T., Yu, H., Ji, Z., Zhong, J., 2021. Ceram. Int. 47, 27609.
Li, D., Qin, W., Zhang, P., Wang, L., Lan, M., 2017. Opt. Mater. Express 7, 1175.
Li, K., Van Deun, R., 2018. Dye. Pigment. 155, 258.
Macedo, H.P., Medeiros Araújo, R.L.B., Medeiros, A.L., Oliveira, Â.A.S., Figueredo, G.P., Freitas Melo, M.A., Araújo Melo, D.M., 2017. Mater. Res. 20, 29.
Mahajan, R., Kumar, S., Prakash, R., Kumar, V., 2018. AIP Conf. Proc. 1953, 1.
Mekprasart, W., Boonyarattanakalin, K., 2018. Mater. Today Proc. 5, 14126.
Mhlongo, M.R., Koao, L.F., Kroon, R.E., Motaung, T.E., Motloung, S.V., 2019. J. Mol. Struct. 1184, 92.
Moji, R.G., Kroon, R.E., Motloung, S.V., Motaung, T.E., Ahemen, I., Koao, L.F., 2020. Mater. Chem. Phys. 242, 122409.
Molefe, F.V., Koao, L.F., Dolo, J.J., Dejene, B.F., 2014. Phys. B Condens. Matter 439, 185.
Motloung, S.V., Dejene, F.B., Swart, H.C., Ntwaeaborwa, O.M., 2014. J. Sol-Gel Sci. Technol. 70, 422.
Motloung, S.V., Dejene, F.B., Swart, H.C., Ntwaeaborwa, O.M., 2015. Ceram. Int. 41, 6776.
Motloung, S.V., Dejene, F.B., Ntwaeaborwa, O.M., Swart, H.C., 2015. Mater. Res. Express 47 (1), 529.
Motloung, S.V., Dejene, F.B., Kroon, R.E., Swart, H.C., Ntwaeaborwa, O.M., 2015. Phys. B Condens. Matter 468–469, 11.
Motloung, S.V., Tsega, M., Dejene, F.B., Swart, H.C., Ntwaeaborwa, O.M., Koao, L.F., Motaung, T.E., Hato, M.J., 2016. J. Alloys Compd. 677, 72.
Motloung, S.V., Dejene, F.B., Koao, L.F., Ntwaeaborwa, O.M., Swart, H.C., Motaung, T.E., Ndwandwe, O.M., 2017. Opt. Mater. (Amst). 64, 26.
Motloung, S.V., Tshabalala, K.G., Kroon, R.E., Hlatshwayo, T.T., Mlambo, M., Mpelane, S., 2019. J. Mol. Struct. 1175, 241.
Ntwaeaborwa, M., Mofokeng, S.J., Kumar, V., Kroon, R.E., 2017. Spectrochim. Acta - Part A Mol. Biomol. Spectrosc. 182, 42.
Pathak, N., Gupta, S.K., Sanyal, K., Kumar, M., Kadam, R.M., Natarajan, V., 2014. Dalt. Trans. 43, 9313.
Rahman, A., Charoo, M.S., Jayaganthan, R., 2015. Mater. Technol. 30, 168.
Sameera, S., Vidyadharan, V., Sasidharan, S., Gopchandran, K.G., 2019. J. Sci. Adv. Mater. Devices 4, 524.
Sampath, S.K., Cordaro, J.F., 2005. J. Am. Ceram. Soc. 81, 649.
Sampath, S.K., Kanhere, D.G., Pandey, R., 1999. J. Phys. Condens. Matter 11, 3635.
Selvi, S., Marimuthu, K., Muralidharan, G., 2015. J. Lumin. 159, 207.
Tangcharoen, T., T-thienprasert, J., Kongmark, C., 2019. J. Adv. Ceram. 8, 352.
Tran, M.T., Trung, D.Q., Tu, N., Anh, D.D., Thu, L.T.H., Du, N.V., Quang, N.V., Huyen, N. T., Kien, N.D.T., Viet, D.X., Hung, N.D., Huy, P.T., 2021. J. Alloys Compd. 884, 1.
Zawadzki, M., Miśta, W., Kępiński, L., 2001. Vacuum 63, 291.
Zhang, Z.J., Feng, A., Chen, X.Y., Zhao, J.T., 2013. J. Appl. Phys. 114.
Zhang, C., Lin, J., 2012. Chem. Soc. Rev. 41, 7938.
Zhang, X., Seo, H.J., 2011. J. Alloy. Compd. 509, 2007.